2D Crystalline Monolayer Nanosheets Produced from 1D-Amorphous Metal-Organic Framework

jiahui wang
Cent S University
Pengfei Yang
Cent S University
Lingmei Liu
King Abdullah University of Science and Technology https://orcid.org/0000-0002-3273-9884
Bin Zheng
Xi'an University of Science and Technology
Jing Jiang
Cent S University
Jian-Ping Ma
Shandong Normal Univ
Yi Yan
Xiangtan Univ
Song Yang
Shandong Normal Univ
Bin Lin
University of Electronic Science and Technology of China
Qi-kui Liu
Shandong Normal Univ
Yu Han
King Abdullah University of Science and Technology https://orcid.org/0000-0003-1462-1118
Yin Chen (chenyin@iccas.ac.cn)
Cent S University

Article

Keywords: Metal-organic-framework, IPM-1, 3D crystalline materials, monolayer nanosheets

DOI: https://doi.org/10.21203/rs.3.rs-45816/v1

Abstract

MOFs are typical 3D crystalline materials, and amorphous MOFs emerges as a new attractive material family very recently. Herein, we report a novel layered MOF, **IPM-1**, which is synthesized from a cage-like organic linker with extremely weak interlaminar interaction. When subjected to external disturbance, **IPM-1** degraded to an intermediate state between the crystalline and amorphous phase (1D-amorphours), in which the layers retain the in-plane two-dimension periodic structure but are misaligned in the third dimension, leading to the loss of apparent porosity and crystallinity. 1D-amorphous **IPM-1** is readily exfoliated into crystalline 2D nanosheets with a thickness of 1.15 nm at gram-scale, excellent uniformity and homogeneity, lateral size up to 10 μm, and restored microporosity. They can fabricate wafer-scale thin films and present the first mass-producible 2D monolayer material. This work underlines that MOFs without apparent crystallinity can be idea precursors for the successful preparation of 2D crystalline monolayer nanosheets.

Main Text

MOFs are organic-inorganic hybrid crystalline materials with well-defined pores of molecular dimensions.[1-6] Compared with 3D MOF crystals, two-dimensional (2D) MOF nanosheets have higher flexibility and surface area, better processability, and more easily accessible active sites, which are particularly advantageous for applications requiring continuous defect-free pore structures, such as molecular sieving, separation, sensing and catalysis.[7-12] Although we share a library with more than 60, 000 kinds of MOFs, only very limited number of 2D MOF nanosheets have been prepared *via* top-down exfoliation[12-15]or bottom-up synthesis.[16,17] In most cases, however, the obtained MOF nanosheets have uneven thicknesses, limited lateral sizes, many defects and low production yields. It remains a great challenge to prepare uniform MOF nanosheets with a well-defined molecular thickness at large scale.

It is conceivable that layer-structured MOFs can be used to produce 2D MOF sheets by mechanical or chemical exfoliation, which is the most common and effective way for the production of 2D materials.[13,18-20] The success of this strategy relies on the strong in-plane linkages coupled with weak interlaminar (out-of-plane) interaction, which ensures that the cleavage of the parent layered crystal occurs along the desired direction. Direction-specific interactions can be introduced into MOFs by rationally designed synthesis.

From the physics point of view, in the liquid exfoliation process of the layered 3D crystals, the 2D layers in the lattice are subjected to shear force (F_s) and interlaminar interaction ( ) (Fig. 1A). In the moment $F_s >$, the interlayer slippages and layer separation occur, which results in the formation of nanosheet. The collision momentum component parallel to the layer plus the viscous force equal to F_s, which tends to separate the layers (Fig. S1, S2; Equation S1), and the component vertical to the layers tends to tear the layers into smaller pieces. F_s can be greatly enhanced by sonication along the direction of the power

source (detailed information in SI, around 1E-10 - 1E-8 N for 1 nm^2 real force area). F_i equals to the summation of pairwise interactions between adjacent layers (Equation S2), which depends on the strength and number of the pairwise interaction in unit area (detailed information in SI). Its component parallel to the layer plane competes against F_s to avoid exfoliation,[21] and the value was calculated as 6E-9 N for graphene in 1 nm^2 contact area.

Obviously, to make the layer exfoliation possible, we need to decrease the value and increase the F_s value. Specifically, three key factors should be considered. At first, the bulk crystals should have layered structure and weak interlaminar interaction so as to achieve the key criterion $F_s >$. In the second, F_s value is positively correlated with the external driving force (v_s) and real force area $l \bullet h \bullet (1+\Delta \bullet w)$. As such, thicker layer (h) and porous structure (Δ) can effectively enhance F_s. At last, the layer should be mechanically strong so as to avoid damage caused by the vertical component of collision momentum, which can be mitigated with porous structure.

Even though only weak intermolecular interactions (Van der Waals force, π-π stacking, CH-π interaction *etc.*) exist between the layers, [7,10,15,22-25] the significant number of densely arranged bonding sites give rise to sufficient interaction force to lock the periodical position of the 2D layers in the crystal lattice,[26] which presents the biggest hurdle for the production of monolayer nanosheets and its commercial applications.[27-29] Weakening the interlaminar interaction in layered MOFs is the ultimate solution and requires a rational design to substantially reduce the bonding energy and the number of bonding sites in unit area.

Paradoxically, sufficiently weak interlayer binding may cause relative sliding between layers, leading to disordered stacking and thus the loss of structural periodicity in one-dimension (Fig. 1B); Consequently, the resulting materials do not show diffraction peaks in conventional in-house powder X-ray diffraction (XRD) characterization, and thus may be considered amorphous. Unlike the recently reported amorphous MOFs (*a*MOFs), an emerging function material family with great application potential,[30-33] are amorphized MOFs by introduction of disorder into the parent crystalline frameworks through heating, pressure (both hydrostatic and nonhydrostatic), and ball-milling. They are amorphous in three-dimensions instead of in one-dimension and lack any long-range periodic order.

Cage-like molecules have been used as idea building blocks to construct porous 3D layered structures with weak interlaminar interaction.[34-36] Bicyclocalix[2]arene[2]triazines tri-carboxylicacid (**BCTA**), a cage-like D_3h symmetric molecule (Fig. 1C),[37] can self-assemble into 3D layered structure with big pores. An interesting feature of the obtained layered structure is that, there are only very weak and scattered interaction pairs between the layers (Fig. S2). The enclosed calixarene cavities and rigid structure of **BCTA** brings molecular recognition properties and inherent micropores,[38-40] and reduces the real contact area between layers. Taking advantage of this feature, we fabricate a layered MOF (denoted as **IPM-1**) using **BCTA** to achieve weak interlaminar interaction. We demonstrate that **IPM-1** comprises highly crystalline monolayers stacked in a disordered manner, differing from both traditional “crystalline” and

“amorphous” phase. Furthermore, the weak interlaminar interaction enables facile exfoliation of **IPM-1** into uniform, molecularly thin 2D MOF sheets with a rather high yield by simple treatment. Our study not only provides an effective strategy for designing precursor materials of truly 2D MOFs, but also highlights an important intermediate state between traditional “crystalline” and “amorphous”, revealing that seemingly unsuccessful products may be highly useful.

IPM-1 was prepared from **BCTA** and $MnCl_2$ in N,N-dimethylformamide (DMF) (Fig. S3-S6). **IPM-1** easily loses 3D crystallinity in the ambient environment and its crystal structure can only be solved by low-temperature single crystal X-ray diffraction performed at -80 ^{o}C. As the single crystal structure shown in Fig. 2A, it clearly indicates that **IPM-1** has a separated layered structure with a layer thickness of 1.15 nm, which is nearly double the height of **BCTA** (Fig. S2, S7A). In the single layer, this network is very rigid with high mechanical strength topologically, extending in the *ac* plane with three types of regular pores (the pore sizes are 0.8nm, 1.3nm, and 1.5nm, Fig. 2B). In the crystal lattice, there are two types of $[Mn_3(O_2C)_6]$ clusters, i.e., $[Mn_3(O_2C)_6]·4H_2O$ and $[Mn_3(O_2C)_6]·2H_2O·2DMF$, arranged into two alternatively-arranged rows in the layer plane, as shown in Fig. S7B. These two types of $[Mn_3(O_2C)_6]$ clusters are connected by trigeminal **BCTA** ligands to form a 2D network with 3,6-connected net nodes (Schläfli symbol {4^3}2{4^6;6^6;8^3}, with very high structural stability, Fig. 2C).

Along the [0, -1, 1] axis, one single **IPM-1** layer looks like a square-wave, similar to black-phosphorus monolayer in some extent. The net-like layers stacked in a ABAB arrangement along the crystallographic *b* axis *via* very weak interlayer O–H···O hydrogen bonding [$d_{O\text{-}H\ldots O}$ = 2.618 and 2.404 Å] between these two different $[Mn_3(O_2C)_6]$ clusters, whereby these hydrogen bonding are the sole interaction between the layers (Fig. 2A, S7C). This results in a 3D neutral supramolecular framework with three ellipsoid channels as illustrated in Fig. 2D, S8. There are two types of regular rectangle channels that exist between the square-wave layers for a half-phase difference (the sizes are 1.3*0.5 nm and 1.3*0.2 nm respectively, Fig. S9). All these channels vertical or parallel to the layer surface have significantly reduced the number of the weak hydrogen-bonding in unit area between adjoining layers. Meanwhile, the 3D crystal is stabilized by an interlocking structure, which is an interpenetrating network formed by the coordinated DMF molecules on $[Mn_3(O_2C)_6]$ clusters (Fig. 1E). In brief, the extremely low interlaminar interaction discovered in **IPM-1** crystal makes it a perfectly candidate for our experiment.

Scanning electron microscopy (SEM) images have confirmed that the apparent structure of **IPM-1** is highly consistent with the single crystal data, very distinct and smooth layered structure was observed(Fig. 3A, S10). Tapping-mode atomic force microscopy (AFM) and transition electron microscopy (TEM) images confirmed that **IPM-1** is readily exfoliated into monolayer nanosheets in the gram-scale *via* simple ultrasonic exfoliation (Fig S11-S13). These monolayer nanosheets have unprecedent evenness and homogeneity. **IPM-1** nanosheets can be prepared by routine ultrasonication treatment in different solvents (Fig S14). The as-prepared colloidal suspension remained stable at room temperature for several months, with significant Tyndall effect (Fig. 3A inset).

With the high concentration nanosheets suspension, AFM images show plenty of rigid and high flatness nanosheets (~ 0.1- 0.2 mg/ml, Figure 3B, S12), with a lateral size range from several to more than ten micrometres. A large-size wafer was produced on the substrate with a thickness of 1-2 nm from a 1-5 μg/ml nanosheets suspension (Fig. S13). As demonstrated by the AFM analyses on forty-three different sites (Fig. 3C, S13), more than 90% of them had a thickness of 1.1±0.2nm, which confirms that the nanosheets are presented as monolayer with high homogeneity. Fig. 3D shows an enlarged area of the dispersed nanosheet. The height profile reveals that the nanosheet is extremely flat, with an even step height of 1.1 nm that is consistent with the thickness of the monolayer in crystal structure. The infrared spectrum of the nanosheets prepared in a large-batch is in good agreement with that of the freshly-prepared IPM-1 crystal (Fig. S15), stronger and more distinct absorbance bands were observed for nanosheets in the fingerprint 1300-700 cm^{-1} region. Thus, it can be concluded that the chemical structure of **IPM-1** remains stable during the exfoliation process. The rigid and smooth appearance of **IPM-1** nanosheets identified a high mechanical strength, as ultrathin nanosheets easily curled under such conditions.

The crystallinity of **IPM-1** nanosheets was directly evidenced by low-dose high-resolution TEM (HR-TEM).[41,42] Lattice fringes are clearly observed in the HR-TEM image with the information transfer up to ~4 Å (Fig. 3E, S16). The fast Fourier transform (FFT) pattern of the HR-TEM image (Fig. 3G) matches reasonably well with the simulated electron diffraction pattern of IPM-1 along the [001] direction (Fig. 3F, based on the CIF of **IPM-1** monolayer). The three labelled spots correspond to the 110 (1.96 nm), 010 (2.09 nm), and 100 (2.02 nm) reflections, respectively. These experimental results indicate the preservation of high crystallinity in the 2D nanosheet after the exfoliation process and the retention of the monolayer structure observed in crystal.

The bulk **IPM-1** crystals appear highly “unstable” according to XRD. The powder XRD pattern of freshly prepared **IPM-1** sample can be fitted to the simulated one (Fig. 4A), but **IPM-1** is considered as an “amorphous” material according to XRD after various regular treatments such as heating, drying or solvent soaking (Fig. 4B). However, it should be noted that there is no change in the crystal appearance (Fig. S17). Generally speaking, it is commonly believed that there is no long-range order in an amorphous material. Very recently, evidences show that the zeolitic imidazolate framework (ZIF) glass does not even have short-range periodicity.[43] However, the experimental results already confirmed the stability and 2D crystallinity of **IPM-1**. It is obviously a deviation from the ordinary which cannot be explained using the current X-ray crystallography.

In the regular treatments, the coordinated DMF in the **IPM-1** crystal lattice dissociated, leading to the degradation of the interlocking structure. The calculated for **IPM-1** is around 2E-10 N per nm^2 contact area based on the single crystal structure. The thermal motion of the solvent molecules in **IPM-1** channels gives rise to a weak F_s due to fluctuation, which can reach the same scale as in a small region (see SI), leading to random interlayer slippage. The crystal lattice lost the atomic periodicity in one dimension in turn. However, this slippage still is localized, as a significant number of hydrogen bonding between the

layers keep the **IPM-1** "crystal" stable. Under sonication exfoliation condition, the 1.15 nm layer thickness and porous structure promoted the F_s to 1E-9 - 1E-8 N per nm^2 scale. The large-pore structure can effectively reduce the damage to the nanosheet. Hence, **IPM-1** has successfully been exfoliated into the observed monolayer nanosheets in gram scale with large lateral size and high homogeneity.

IPM-1 is thermally stable up to 440 ^oC (Fig. S6), and has a BET surface area of 210 m^2/g and a CO_2 absorption of 41 cm^3/g after activation at 150 ^oC under vacuum (As shown in Fig. 4C, 4D). IPM-1 has a typical type I N_2 adsorption-desorption isotherm. The adsorption was apparent in the low-pressure region ($P/P_0 < 0.05$) and the desorption of N_2 was reversible with an observable hysteresis. **IPM-1** nanosheet has nearly a doubled BET surface area (360 m^2/g) and CO_2 absorption (58 cm^3/g) as compared to bulk **IPM-1** (BET and CO_2 absorption were performed with 130 mg **IPM-1** nanosheets, as shown in inset of Fig. 4E). It is known that heterocalixaromatics can bind to CO_2 *via* its nitrogen-rich cavities.[44] Thus, the availability of the fully exposed calixarene cavities in **IPM-1** nanosheet leads to this remarkable CO_2 absorption observed. More importantly, while bulk **IPM-1** show a broad and ambiguous pore size distribution, the pore size distribution for **IPM-1** nanosheet is highly distinct (Fig. 4E), which is identical to the theoretical values as shown in Fig. 2B. This could be attributed to the removal of the irregular pores in the bulk **IPM-1** as a result of interlayer slippage after complete separation, and no BET hysteresis was observed in the N_2 desorption isotherm of the **IPM-1** nanosheet (Fig. 4C).

High pressure BET test results show that the blocked channels and calixarene cavities in **IPM-1** could be opened at high pressure. At 273 K, when the pressure reached 60 atm (maximum pressure of 200 atm), N_2 absorption of **IPM-1** increased from 2.8 cm^3/g to 7.0 cm^3/g (the interaction between N_2 molecules and the frameworks is very weak). Meanwhile, the CO_2 absorption (performed with the same batch sample) increased from 18 cm^3/g to 56 cm^3/g at 38 atm (Fig. 4E). Both desorption revealed hysteresis, but they were reversible at reduced pressure, which confirmed the high structural stability of **IPM-1** layers. [45,46]

It can be concluded from the above experimental results: **IPM-1** exhibits a good physical and chemical stability, and it is 1D-amouphous due to the localized interlayer slippage, which presents an intermediate phase between the classic crystalline and amorphous phase. The interlayer slippage leads to the blockage of the channels and micropores instead of structure collapsing. After exfoliation, **IPM-1** nanosheets possess high macroscopic homogeneity and restored microporosity. In addition, the stacking fault caused by the interlayer slippage in **IPM-1** is variable at the angstrom scale. More interestingly, neither aggregation of nanosheets nor crystalline phase recovery has been detected with the as-prepared nanosheets. This cheap, easy, and scalable preparation of **IPM-1** monolayer nanosheets can further render its commercialization highly feasible.

Why **IPM-1** has been determined as "amorphous" by in-house XRD characterization? As we know, the molecules are in chaotic thermal motion within the confined space of the crystal lattice, which leads to the loss in the periodicity. If the initial distance between two adjacent molecules is set as ε(0), after time *t*, the distance can be described as (, the Lyapunov exponent, Fig. 1A, S18).[47,48] For an effective diffraction

crystal plane with n atoms, the detection error will be amplified by times. In an ideal close packed crystal, the thermal motion is confined in picometers scale, but the wavelength of the X-ray generally used in XRD is around 1 Å. Therefore, the influence of this kind of thermal motion to XRD observation is limited. In addition, the lattice wave makes the atoms correlated in long range, , $\lambda \rightarrow 0$, the error in the diffraction crystal planes can be omitted.

In **IPM-1**, experimental results indicate that the movement of the atoms along the layer plane can increase to angstrom scale due to the interlayer slippage. Given a 2 Å $\varepsilon_{(max)}$, the $\lambda_{IPM\text{-}1}$ can reach 0.1 in the crystal lattice (λ value is decided by). The corresponding detection error will increase times, resulting in an extremely poor S/N ratio.

In this study, a 1D-amouphous MOF, **IPM-1**, is designed and prepared. Experimental results verified its in-plane 2D periodic structure and misaligned arrangement in the last dimension, which is similar to the quasicrystal in some extent,[49] as they are both partially periodical in atomic arrangement. This intermediate state can be attributed to the extremely low interlaminar interaction and the resulting localized interlayer slippage. The exfoliated **IPM-1** nanosheet presents the first mass-producible 2D monolayer MOF nanosheet, and exhibits high uptake capacity and selectivity for CO_2 adsorption. In addition, the “amorphous” status observed in **IPM-1** may be vital towards the successful preparation of monolayer 2D material.

Declarations

Acknowledgments:

Y.C. thanks Prof. Jean-Pierre Sauvage, Enrico Traversa, Jean-Marie Basset, Yi Zhang, Min Liu, Bo Tang, Yu-Bin Dong, Guo-Xia Jin, Tao Yue, Hai Xu for the helpful discussion. **Funding**: Y. C. thanks the financial support from Central South University, NSF of China. **Author contributions**: Y. C., Y. H. and Q. L. conceived the experiments. Y.C. supervised the research. J.W. developed the material synthesis. P. Y. performed the nanosheets exfoliation and corresponding characterizations. L.L. performed the HR-TEM characterization. B. Z. performed the DFT calculation and the crystal structure simulation. J. J., Y. Y., S. Y. and L. Y. performed part of the synthesis and characterizations. J. M. contributed to the scientific discussion and crystal data analysis. Y.C., Y.H. and B.L. wrote the manuscript. All authors discussed the results and commented on the manuscript. **Competing interests**: The authors declare no competing financial interests.

References

1. Furukawa, H., Cordova, K. E., O'Keeffe, M. & Yaghi, O. M. The Chemistry and Applications of Metal-Organic Frameworks. *Science* **341**, 974-+, doi:10.1126/science.1230444 (2013).
2. Horike, S., Shimomura, S. & Kitagawa, S. Soft porous crystals. *Nat. Chem.* **1**, 695–704, doi:10.1038/nchem.444 (2009).

3. Gu, C. *et al.* Design and control of gas diffusion process in a nanoporous soft crystal. *Science* **363**, 387–391, doi:10.1126/science.aar6833 (2019).
4. Eddaoudi, M. *et al.* Systematic design of pore size and functionality in isoreticular MOFs and their application in methane storage. *Science* **295**, 469–472, doi:10.1126/science.1067208 (2002).
5. Inokuma, Y. *et al.* X-ray analysis on the nanogram to microgram scale using porous complexes. *Nature* **495**, 461-+, doi:10.1038/nature11990 (2013).
6. Cadiau, A., Adil, K., Bhatt, P. M., Belmabkhout, Y. & Eddaoudi, M. A metal-organic framework-based splitter for separating propylene from propane. *Science* **353**, 137–140, doi:10.1126/science.aaf6323 (2016).
7. Peng, Y. *et al.* Metal-organic framework nanosheets as building blocks for molecular sieving membranes. *Science* **346**, 1356–1359, doi:10.1126/science.1254227 (2014).
8. Rodenas, T. *et al.* Metal–organic framework nanosheets in polymer composite materials for gas separation. *Nat. Mater.* **14**, 48, doi:10.1038/nmat4113 (2014).
9. Liu, Y. *et al.* Van der Waals heterostructures and devices. *Nature Reviews Materials* **1**, 16042, doi:10.1038/natrevmats.2016.42 (2016).
10. Wang, X. *et al.* Reversed thermo-switchable molecular sieving membranes composed of two-dimensional metal-organic nanosheets for gas separation. *Nat. Commun.* **8**, 14460, doi:10.1038/ncomms14460 (2017).
11. Zhang, C., Wu, B.-H., Ma, M.-Q., Wang, Z. & Xu, Z.-K. Ultrathin metal/covalent-organic framework membranes towards ultimate separation. *Chem. Soc. Rev.* **48**, 3811–3841, doi:10.1039/c9cs00322c (2019).
12. Zhao, M. *et al.* Two-dimensional metal-organic framework nanosheets: synthesis and applications. *Chem. Soc. Rev.* **47**, 6267–6295, doi:10.1039/c8cs00268a (2018).
13. Tan, C. *et al.* Recent Advances in Ultrathin Two-Dimensional Nanomaterials. *Chem. Rev.* **117**, 6225–6331, doi:10.1021/acs.chemrev.6b00558 (2017).
14. Ding, Y. *et al.* Controlled Intercalation and Chemical Exfoliation of Layered Metal–Organic Frameworks Using a Chemically Labile Intercalating Agent. *J. Am. Chem. Soc.* **139**, 9136–9139, doi:10.1021/jacs.7b04829 (2017).
15. Huang, J. *et al.* Electrochemical Exfoliation of Pillared-Layer Metal-Organic Framework to Boost the Oxygen Evolution Reaction. *Angewandte Chemie-International Edition* **57**, 4632–4636, doi:10.1002/anie.201801029 (2018).
16. Junggeburth, S. C. *et al.* Ultrathin 2D Coordination Polymer Nanosheets by Surfactant-Mediated Synthesis. *J. Am. Chem. Soc.* **135**, 6157–6164, doi:10.1021/ja312567v (2013).
17. Zhong, Y. *et al.* Wafer-scale synthesis of monolayer two-dimensional porphyrin polymers for hybrid superlattices. *Science* **366**, 1379–1384, doi:10.1126/science.aax9385 (2019).
18. Cai, X. K., Luo, Y. T., Liu, B. & Cheng, H. M. Preparation of 2D material dispersions and their applications. *Chem. Soc. Rev.* **47**, 6224–6266, doi:10.1039/c8cs00254a (2018).

19. Nicolosi, V., Chhowalla, M., Kanatzidis, M. G., Strano, M. S. & Coleman, J. N. Liquid Exfoliation of Layered Materials. *Science* **340**, 1420-+, doi:10.1126/science.1226419 (2013).
20. Geim, A. K. & Novoselov, K. S. The rise of graphene. *Nat. Mater.* **6**, 183–191, doi:10.1038/nmat1849 (2007).
21. Israelachvili, J. N. *Intermolecular and surface forces*. (Academic press, 2015).
22. Hermosa, C. *et al.* Mechanical and optical properties of ultralarge flakes of a metal-organic framework with molecular thickness. *Chemical Science* **6**, 2553–2558, doi:10.1039/c4sc03115f (2015).
23. Au, V. K.-M. *et al.* Stepwise Expansion of Layered Metal-Organic Frameworks for Nonstochastic Exfoliation into Porous Nanosheets. *J. Am. Chem. Soc.* **141**, 53–57, doi:10.1021/jacs.8b09987 (2019).
24. Novoselov, K. S., Mishchenko, A., Carvalho, A. & Castro Neto, A. H. 2D materials and van der Waals heterostructures. *Science* **353**, aac9439 doi:10.1126/science.aac9439 (2016).
25. Liu, Y., Huang, Y. & Duan, X. F. Van der Waals integration before and beyond two-dimensional materials. *Nature* **567**, 323–333, doi:10.1038/s41586-019-1013-x (2019).
26. Lehn, J.-M. Supramolecular chemistry. *Science* **260**, 1762–1764, doi:10.1126/science.8511582 (1993).
27. Shim, J. *et al.* Controlled crack propagation for atomic precision handling of wafer-scale two-dimensional materials. *Science* **362**, 665-+, doi:10.1126/science.aat8126 (2018).
28. Deng, Y. *et al.* Gate-tunable room-temperature ferromagnetism in two-dimensional Fe3GeTe2. *Nature* **563**, 94-+, doi:10.1038/s41586-018-0626-9 (2018).
29. Novoselov, K. S. Rapid progress in producing graphene. *Nature* **505**, 291–291, doi:10.1038/505291c (2014).
30. Bennett, T. D. & Cheetham, A. K. Amorphous Metal–Organic Frameworks. *Acc. Chem. Res.* **47**, 1555–1562, doi:10.1021/ar5000314 (2014).
31. Bennett, T. D. *et al.* Structure and Properties of an Amorphous Metal-Organic Framework. *Phys. Rev. Lett.* **104**, doi:10.1103/PhysRevLett.104.115503 (2010).
32. Bennett, T. D. & Horike, S. Liquid, glass and amorphous solid states of coordination polymers and metal–organic frameworks. *Nature Reviews Materials* **3**, 431–440, doi:10.1038/s41578-018-0054-3 (2018).
33. Liu, C. *et al.* Amorphous Metal–Organic Framework-Dominated Nanocomposites with Both Compositional and Structural Heterogeneity for Oxygen Evolution. **59**, 3630–3637, doi:10.1002/anie.201914587 (2020).
34. Zhang, C. *et al.* A Porous Tricyclooxacalixarene Cage Based on Tetraphenylethylene. *Angewandte Chemie International Edition* **54**, 9244–9248, doi:10.1002/anie.201502912 (2015).
35. Kissel, P., Murray, D. J., Wulftange, W. J., Catalano, V. J. & King, B. T. A nanoporous two-dimensional polymer by single-crystal-to-single-crystal photopolymerization. *Nat. Chem.* **6**, 774–778,

doi:10.1038/nchem.2008 (2014).

36. Kory, M. J. *et al.* Gram-scale synthesis of two-dimensional polymer crystals and their structure analysis by X-ray diffraction. *Nat. Chem.* **6**, 779–784, doi:10.1038/nchem.2007 (2014).
37. Chen, Y., Wang, J., Hai, X., Li, Q. & Jiang, J. Facial one-pot synthesis of D-3 h symmetric bicyclocalix 2 arene 2 triazines and their layered comb self-assembly. *Journal of Saudi Chemical Society* **22**, 628–635, doi:10.1016/j.jscs.2017.11.003 (2018).
38. Wang, M.-X. Nitrogen and Oxygen Bridged Calixaromatics: Synthesis, Structure, Functionalization, and Molecular Recognition. *Accounts of Chemical Research* **45**, 182–195, doi:10.1021/ar200108c (2012).
39. Zhang, G. & Mastalerz, M. Organic cage compounds - from shape-persistency to function. *Chemical Society Reviews* **43**, 1934–1947, doi:10.1039/c3cs60358j (2014).
40. Mitra, T. *et al.* Molecular shape sorting using molecular organic cages. *Nature Chemistry* **5**, 276–281, doi:10.1038/nchem.1550 (2013).
41. Zhang, D. *et al.* Atomic-resolution transmission electron microscopy of electron beam-sensitive crystalline materials. *Science* **359**, 675-+, doi:10.1126/science.aao0865 (2018).
42. Liu, L. *et al.* Imaging defects and their evolution in a metal-organic framework at sub-unit-cell resolution. *Nat. Chem.* **11**, 622–628, doi:10.1038/s41557-019-0263-4 (2019).
43. Madsen, R. S. K. *et al.* Ultrahigh-field 67 Zn NMR reveals short-range disorder in zeolitic imidazolate framework glasses. *Science* **367**, 1473–1476, doi:10.1126/science.aaz0251 (2020).
44. Wang, Z. *et al.* Networked Cages for Enhanced CO2 Capture and Sensing. *Advanced Science* **5**, 1800141, doi:10.1002/advs.201800141 (2018).
45. Kitaura, R., Seki, K., Akiyama, G. & Kitagawa, S. Porous coordination-polymer crystals with gated channels specific for supercritical gases. *Angewandte Chemie-International Edition* **42**, 428–431, doi:10.1002/anie.200390130 (2003).
46. Zhang, J.-P., Zhou, H.-L., Zhou, D.-D., Liao, P.-Q. & Chen, X.-M. Controlling flexibility of metal-organic frameworks. *National Science Review* **5**, 907–919, doi:10.1093/nsr/nwx127 (2018).
47. Williams, G. *Chaos theory tamed*. (CRC Press, 1997).
48. Chávez-Carlos, J. *et al.* Quantum and Classical Lyapunov Exponents in Atom-Field Interaction Systems. *Phys. Rev. Lett.* **122**, 024101, doi:10.1103/PhysRevLett.122.024101 (2019).
49. Shechtman, D., Blech, I., Gratias, D. & Cahn, J. W. Metallic phase with long-range orientational order and no translational symmetry. *Phys. Rev. Lett.* **53**, 1951 (1984).

Figures

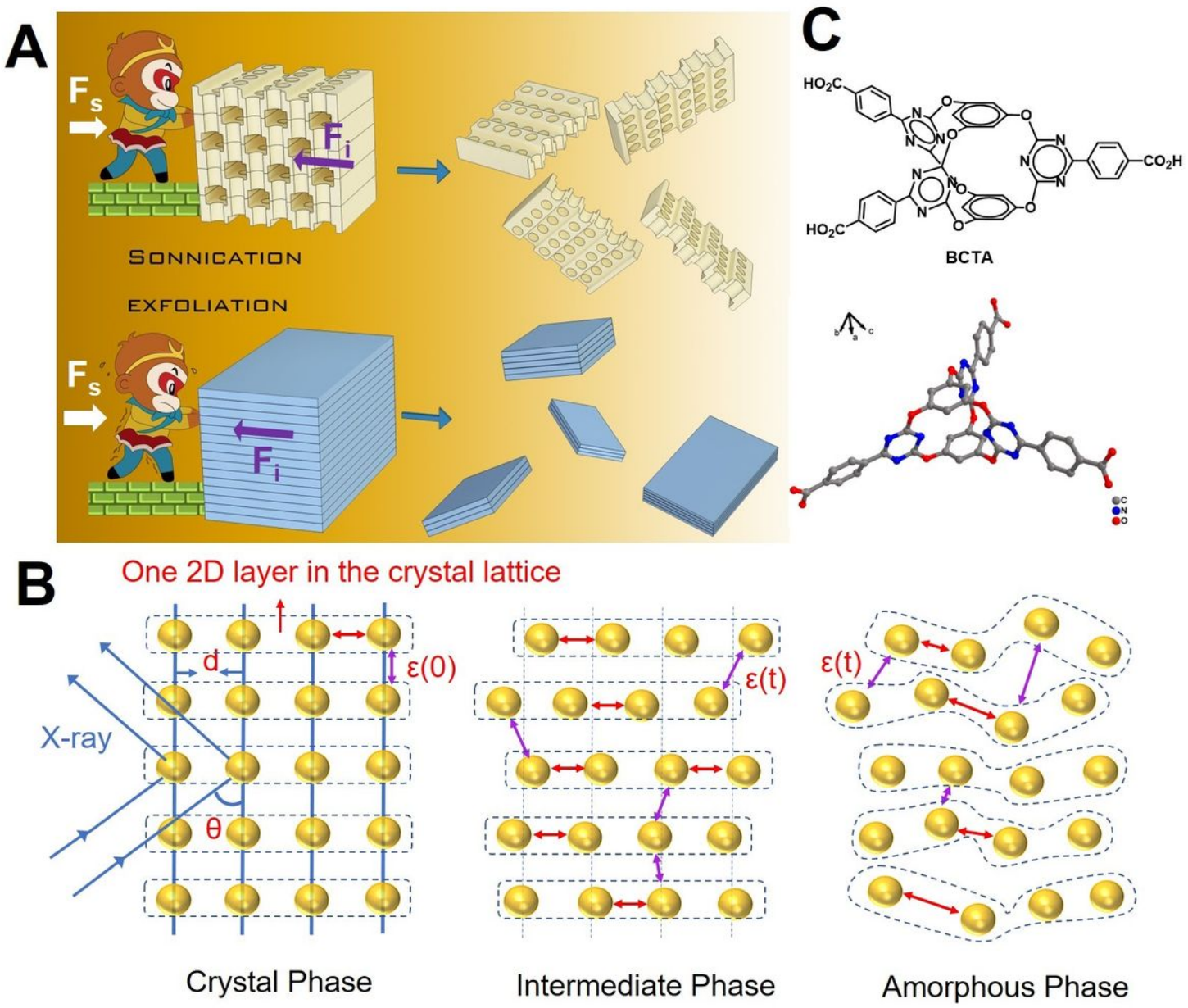

Figure 1

(A) Schematic illustration of the influence of shear force (Fs) and interlaminar interaction (Fi) to the interlayer slippage and exfoliation into nanosheet. (B) Schematic illustration of the 1D-amorphous transition state between the crystal and amorphous phase. The dot arrays present the side projection of the 3D molecular lattice. Golden ball represents the molecules in the lattice; dotted rectangle represents one 2D layer, red double arrow (denoted as ↔) represents the molecular distance in the 2D layer at time (0), while purple double arrow (denoted as ↔) represents the molecular distance between the layers at time (0). Crystalline phase is whereby the molecules are periodical in 3D lattice, which can give X-ray diffraction pattern. Intermediate phase is whereby the aperiodicity in one dimension, and the X-ray diffraction pattern disappears. Amorphous phase is whereby the molecules are aperiodic in all dimensions. (C) The molecular and crystal structure of BCTA.

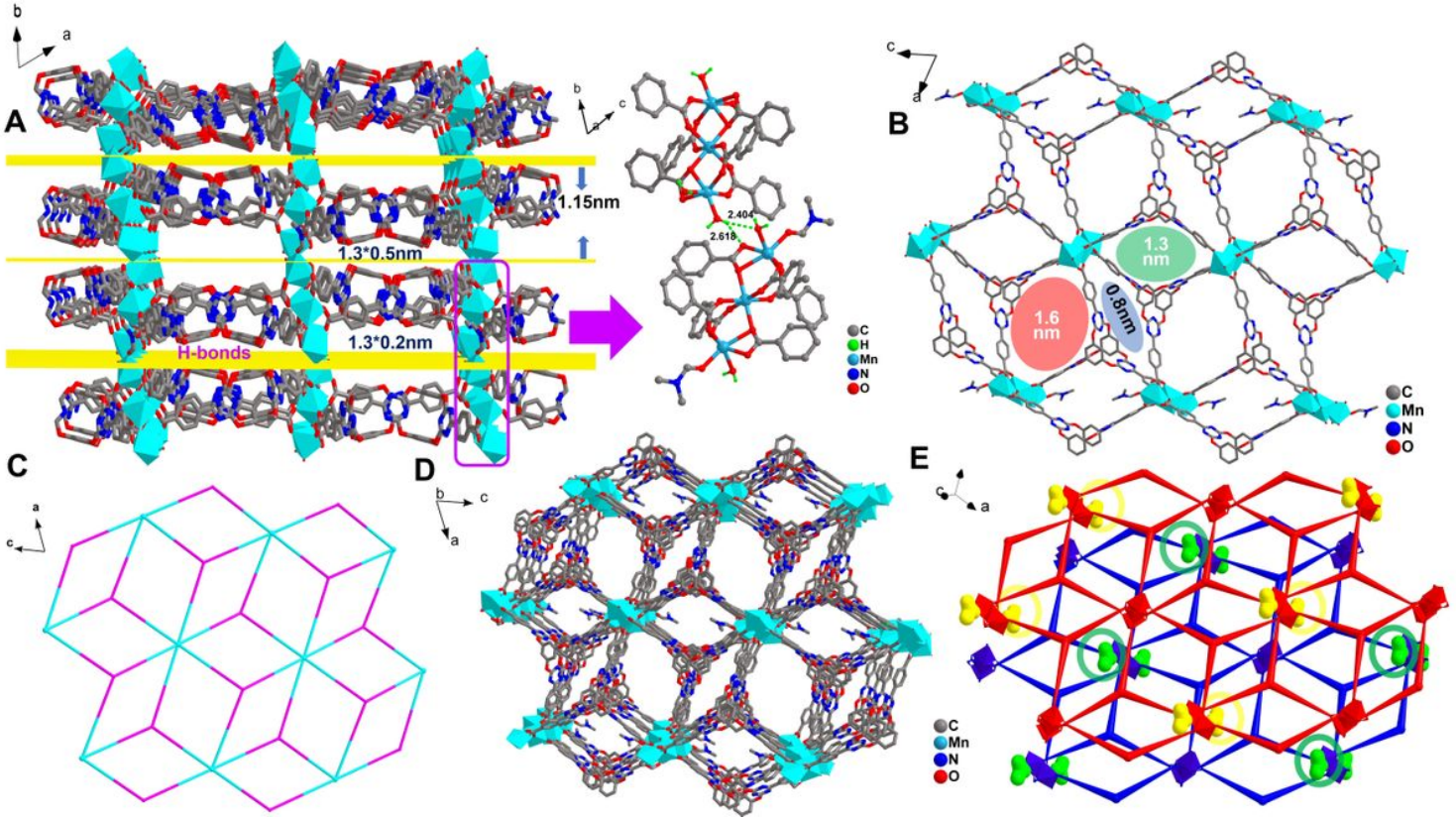

Figure 2

X-ray single crystal structure of the IPM-1. (A) Architecture of the IPM-1 layered structure, with a thickness of 1.15 nm for each layer. Two types of rectangle channels exist between the layers (the sizes are 1.3*0.2 nm and 1.3*0.5 nm respectively). The purple rectangle indicates the only hydrogen-bonding site between the layers (The very weak hydrogen bonding between two adjacent different [Mn3(O2C)6] clusters). (B) The representation of a single layer in IPM-1 and the three types of pores with different sizes. (C) The 3,6-connected net nodes topological structure for a single IPM-1 layer. (D) The ellipsoid channels formed by the packed IPM-1 layers. (E) The interlocking structure between IPM-1 layers in the crystal lattice(layer A in red, layer B in blue), which keeps IPM-1 crystal stable. Yellow (A in B) and green balls (B in A) present the coordinated DMF molecules of one layer wedged in the other layer.

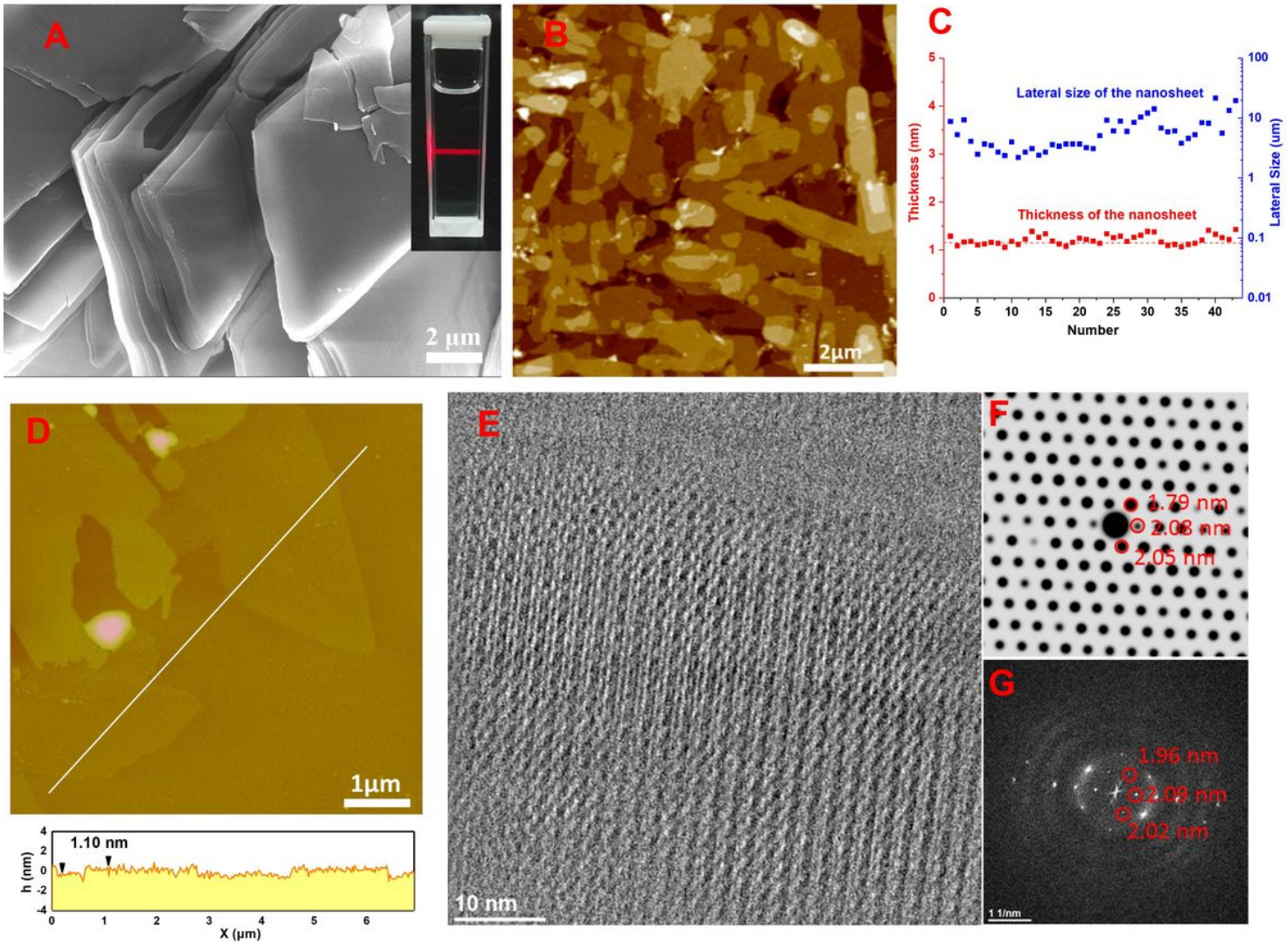

Figure 3

Exfoliation of 2D crystalline IPM-1 monolayer. (A) Scanning electron microscopy (SEM) image of small particle of IPM-1 “crystal” (inset showing the Tyndall effect of the nanosheets colloidal suspension). (B) AFM image of the high concentration IPM-1 nanosheets suspension on freshly cleaved mica surface. (C) Thickness and lateral size distribution of the exfoliated IPM-1 nanosheets (horizontal black dotted line indicates the theoretical thickness of a single layered IPM-1 nanosheets). (D) AFM image of the well-dispersed IPM-1 monolayer nanosheets. The height profile of the nanosheets was recorded along the white lines marked in the AFM image. (E) Low dose high-resolution TEM (HR-TEM) image of IPM-1 nanosheet. (F) The simulated electron diffraction pattern of IPM-1 nanosheet based on the IPM-1 monolayer CIF. (G) The fast Fourier transform (FFT) pattern of IPM-1 nanosheet, which is consistent with the simulated electron diffraction pattern.

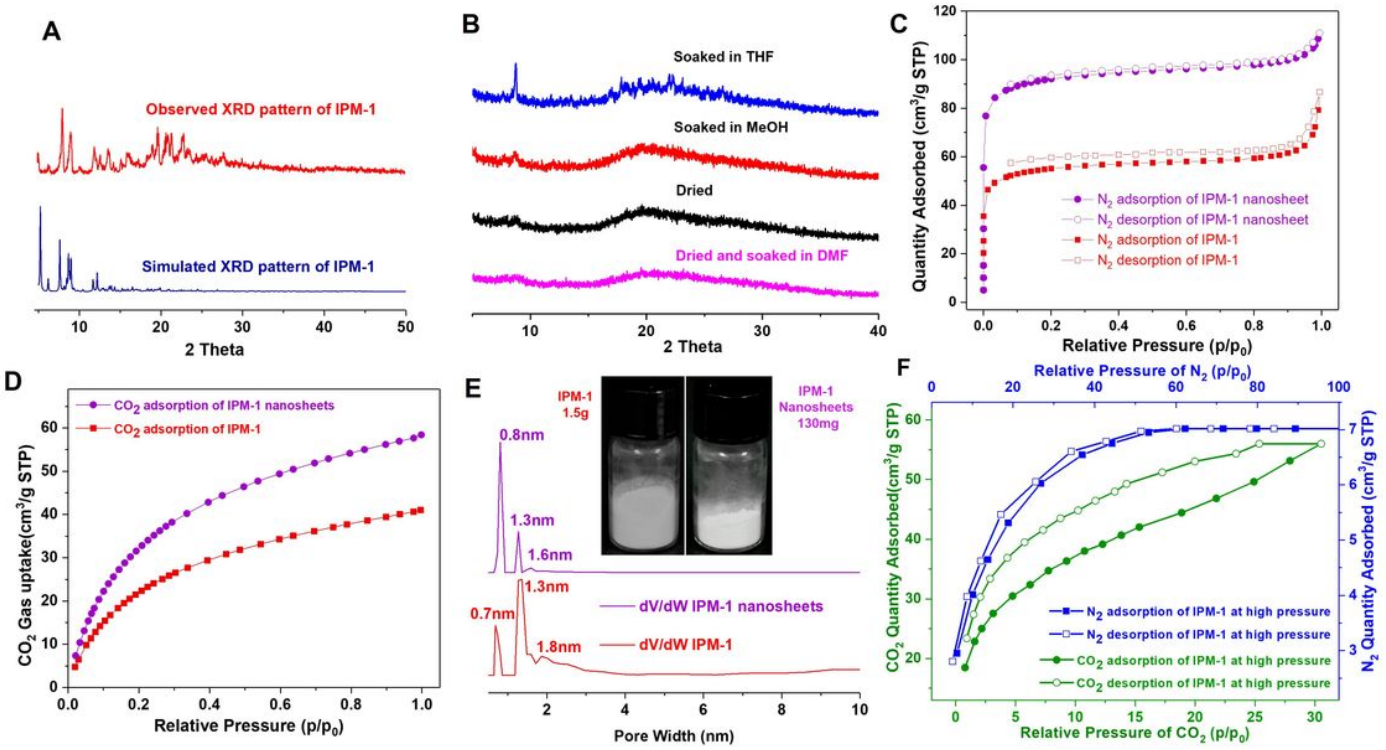

Figure 4

Powder XRD and BET data of IPM-1. (A) Powder XRD pattern of the freshly prepared IPM-1 crystal and the simulated one. (B) Powder XRD pattern of IPM-1 crystal after drying or soaking in other solvent. (C) N2 adsorption-desorption isotherms of IPM-1(red) and IPM-1 nanosheets (purple) at 77 K and various pressures up to 1 bar. (D) CO2 adsorption isotherms of IPM-1(red) and IPM-1 nanosheets (purple) at 273 K and various pressures up to 1 bar. (F) Narrow pore-size distribution of IPM-1 and IPM-1 nanosheet (Inset showing photographs of the comparing between IPM-1 and IPM-1 nanosheets). (E) CO2 (273K) and N2 (298K) adsorption-desorption isotherms of IPM-1 at high pressure.

Supplementary Files

This is a list of supplementary files associated with this preprint. Click to download.

- SupportingMaterial.docx